

Numerical Investigation of the Impact of Intake Pipelines on the Performance and Flow Characteristics of a Centrifugal Compressor

X. Li^{1,2}, N. Huang^{1,2}, W. Han^{3,4}, D. Tong⁵, Y. Zhang⁵ and J. Zhang^{1,2†}

¹ College of Civil Engineering and Mechanics, Lanzhou University, Lanzhou 730000, China

² Key Laboratory of Mechanics on Disaster and Environment in Western China, Lanzhou, Gansu, 730000, China

³ Department of Energy and Power Engineering, Lanzhou University of Technology, Lanzhou 730050, China

⁴ Key Laboratory of Fluid Machinery and Systems, Lanzhou, Gansu, 730050, China

⁵ China North Engine Research Institute, Tianjin, 300400, China

†Corresponding Author Email: zhang-j@lzu.edu.cn

ABSTRACT

Due to the installation space constraints in practical applications, centrifugal compressors often utilize bent intake pipes. Quantifying the correlation between the centrifugal compressor's operating performance and the flow dynamics within curved inlet tubes is essential. In this research, the accuracy of the numerical methodology was validated using the experimental outcomes. Subsequently, the centrifugal compressor's performance was simulated for two intake curved ducts, i.e., P_c with a coplanar central axis and P_{nc} with a non-coplanar central axis, followed by the analysis of the flow characteristics for each intake configuration. The results indicated that P_c produced a symmetrical swirling flow field at the outlet, which was characterized by a lower plane superimposed distortion intensity (*PSDI*), while P_{nc} generated an asymmetrical offset swirling flow field with a higher *PSDI*. The *PSDI* increased with the flow rate, reaching maximum values of 0.137 for P_c and 0.386 for P_{nc} . Compared to the inlet straight tube, the performances of the centrifugal compressor connected to P_c and P_{nc} both decreased, while P_{nc} exhibited a more significant performance deterioration degree. Under high-speed conditions, the maximum degradation degrees of pressure ratio for P_c and P_{nc} reached approximately 5.7% and 9.8%, respectively, while the efficiency reduction degree reached approximately 5.3% and 8.7%, respectively. The performance reduction degree for both bent pipes increased with the rising *PSDI*, exhibiting an exponential correlation. The flow characteristics of the intake pipelines affected the flow behavior within the impeller, with the flow field variation locations closely resembling the distorted regions of the bent pipes.

Article History

Received September 23, 2024

Revised December 17, 2024

Accepted January 17, 2025

Available online March 30, 2025

Keywords:

Centrifugal compressor

Flow characteristics

Plane superimposed distortion intensity

Performance reduction degree

Exponential correlation

1. INTRODUCTION

The advantages of centrifugal compressors such as maintenance convenience, compact structure, and high single-stage pressure ratio (Moosania & Zheng, 2017) have caused them to be widely utilized in industrial applications, including turbochargers and air compression systems (Grimaldi & Michelassi, 2019). As turbochargers are increasingly being employed in power supply systems, the performance requirements for centrifugal compressors are becoming more in demand. However, one practical issue that is encountered is that the spatial constraints alter the intake conditions. Typically, the intake pipeline configuration of the centrifugal compressor is adjusted to fit the installation environment, resulting in a non-axial

symmetric flow condition before the impeller (Li et al., 2020). The discrepancy between actual operating conditions and the design condition of the axial uniform intake leads to variations in the performance, which has drawn considerable attention from researchers.

Earlier studies on compressors operating with asymmetric intake environments mainly focused on axial compressors (Li et al., 2006; Toge & Pradeep, 2017). Due to the extensive adoption of centrifugal compressors, researchers have explored the impact of the uneven flow condition on the operational performance of the centrifugal compressor, primarily through experimental and numerical methods. In related experimental investigations, Ariga et al. (1983) induced asymmetric flow at a centrifugal compressor inlet by modifying the

NOMENCLATURE			
CD	circumferential distortion degree	Q	mass flow rate
P_{at}	atmospheric pressure	SI	Swirling Intensity
P_c	intake bent pipe with coplanar central axis	δ_η	efficiency degradation degree
PCD	circumferential distortion of the plane	δ_π	pressure ratio degradation degree
P_s	straight inlet pipe	η_i	efficiency for inlet bent pipes
$PSDI$	Plane Superimposed Distortion Intensity	η_s	efficiency for straight pipe
PSI	Swirl Intensity of The Plane	π_i	pressure ratio for inlet bent pipes
P_{nc}	intake bent pipe with non-coplanar central axis	π_s	pressure ratio for straight pipe

configuration of a honeycomb distortion generator. Their findings indicated that the asymmetric flow conditions changed the incidence flow angle, leading to a significant decline in the efficiency of the impeller. Kammerer and Abhar (2009) installed distortion screens with different blade configurations upstream of the impeller. Their experimental outcomes measured with aerodynamic probes demonstrated the fact that the distortion screens had a considerable influence on the total pressure distribution upstream of the centrifugal compressor. Kim et al. (2001) discussed the performance parameter of a centrifugal compressor connected to a rectilinear intake duct and a bent tube curved at 90° experimentally. The results showed that the bent pipe negatively affected the compressor's performance, and the researchers found that incorporating a blade structure within the bent tube could improve the flow uniformity. Li et al. (2012) implemented the research on a high-speed centrifugal compressor through experimental technique, evaluating its performance with three different intake pipeline configurations: a straight pipe, a 90° long elbow, and a short elbow. They observed that both bent intake pipes reduced the performance characteristics of the centrifugal compressor, while the long elbow exerted a more negative effect on the performance. Broatch et al. (2018) explored the effect of the curved duct diameter on a turbocharger compressor's performance. The test results indicated that a smaller radius bend altered the efficiency of the compressor and increased the inlet noise intensity near the surge operating point. The experimental findings of Sun et al. (2020) indicated that incorporating an S-shaped intake duct resulted in a performance decline to the centrifugal compressor, with a more serious influence on the flow distribution at the higher flow rate conditions. Additionally, the S-shaped intake pipe had a minimal effect on the compressor's surge margin. With the development of experimental measurement technologies, Particle Image Velocimetry (PIV) techniques have been widely applied in related flow field investigations, and these techniques can be applied to visually monitor the fluid flow patterns (Li et al. 2025). Although the experimental approach was crucial in the related research, it required extended time periods and high costs (Zhang et al., 2001) and was susceptible to limitations from the testing environments and instrumentation.

Recently, the computational fluid dynamics (CFD) approaches have developed rapidly, leading to its extensive adoption across various fields, such as aerospace, automobiles, and mechanical engineering, achieving significant advancements (Yan et al., 2011), as well as wide utilization in the field of fluid machinery (Li et al., 2023a, b). Therefore, numerical simulation has

become a crucial auxiliary tool for analyzing the flow field in compressors (Tian et al., 2017). Numerous researchers have employed this method to examine the effect of distorted flow on the centrifugal compressor. Han et al. (2016) performed numerical simulations to examine the flow losses and the performance variation due to radial intake pipelines. Their results showed that the flow losses and the distorted flow fields within radial intake pipes were the primary factors affecting a shrouded centrifugal compressor's operating performance. Zhao et al. (2017) organized simulations to explore the influence of eight sets of inlet elbows, each with different installation angles, on the alterations of the centrifugal compressor's performance behavior. They concluded that the alteration in the arrangement angle between the volute and curved intake duct affected both the efficiency and the operational stability range of the compressor. Notably, the inlet bent duct with a 135° installation angle along the circumference exhibited the lowest efficiency at high flow rate conditions, indicating that this installation angle should be avoided in practical applications. Jahani et al. (2022) numerically predicted the performance deviations and flow behavior of a centrifugal compressor under inlet boundary conditions with 120° circumferential total pressure distortion. The results demonstrated that the circumferential total pressure distortion reduced the total pressure ratio and the adiabatic efficiency of the impeller by approximately 4% and 2%, respectively. Additionally, tip injection could enhance the flow distribution within the vicinity of the blade tip region. Wang et al. (2023) assessed the aerodynamic performance of a compressor through numerical calculation, comparing the predicted results for the cases with three distinct interstage pipeline configurations. The researchers found that the curved segment of the interstage pipeline led to flow distortion upstream of the impeller entry, while the severity of this distorted flow was found to depend on the structure of the curved tube. Across the multiple configurations, the elbow pipe change (EPC) structure with a uniformly varying inner diameter in the curved section resulted in the highest total pressure distortion at 80 kr/pm. Conversely, the straight pipe change (SPC) model with a constant inner diameter in the curved section exhibited the best performance. Therefore, an SPC-type pipeline is recommended for the installation of two-stage centrifugal compressors. Tong et al. (2021) simulated the performance of a centrifugal compressor with an installation angle of 50° between a 90° inlet bend and volute. The investigation demonstrated that the bent pipe structure induced a deterioration in the pressure ratio and efficiency, primarily in consequence of the uneven flow state at the outlet section of the curved duct. Subsequently,

the researchers improved the flow distribution by arranging a guide vane inside the elbow, leading to a corresponding improvement in the compressor's performance, with the maximum pressure ratio and efficiency increased by approximately 3% and 2.5%, respectively.

Clarifying the impact of non-symmetrical flow conditions produced by varying intake pipelines on the performance of the compressor is beneficial for guiding the design and selection of the inlet ducts. Previous studies on asymmetric flow in centrifugal compressors have primarily examined cases where the central axis of the inlet pipe and the compressor's inlet are in the same plane, such as studies of 90° and 180° bends (Broatch et al., 2018; Sun et al., 2020), which predominantly examined the distortion in total pressure upstream of the compressor. Due to constraints of the installation space, the central axis of an intake pipe and a compressor's entrance are not aligned on the same axial plane in certain environments. These types of intake systems cause variations in the flow direction, leading to both nonuniform total pressure distribution and swirling distortion at the inlet of the compressor (Sheoran et al., 2011). Currently, there is limited exploration on the influence of this type of curved inlet tube on the performance parameter of centrifugal compressors. Moreover, there is a lack of investigations quantifying the combined effects of swirling distortion and total pressure distortion formed by different inlet elbows, as well as their quantitative correlation with the operational performance of a centrifugal compressor.

In this investigation, two structures for intake bent pipes were established, one with a coplanar central axis and the other with a non-coplanar central axis for the intake elbow and the compressor's inlet, namely, P_c and P_{nc} . Then, the study examined the effect of the curved inlet tubes on the operational performance of the target centrifugal compressor. The findings revealed the variations in flow distribution at the compressor inlet with different types of inlet bent ducts. Furthermore, the extent of the flow distortion related to the total pressure and swirling flow at the pipeline outlet was quantitatively assessed, along with the establishment of the quantitative correlation between the magnitude of distortion and the compressor's performance. The research findings can offer valuable guidance for the selection of inlet pipelines and provide theoretical foundation for future efforts to improve asymmetric flow of centrifugal compressor.

The organization of this investigation is outlined as follows. Section 2 presents descriptions of the numerical method, fundamental equations, and the computational mesh. Section 3 describes how the computational methodology was experimentally verified and how the numerically simulated results of the centrifugal compressor were analyzed connected to different curved ducts. Then, the flow field within the impeller is discussed in Section 4, followed by the conclusions in Section 5.

2. ESTABLISHMENT OF THE NUMERICAL SIMULATION

The aim of this research was a turbocharged

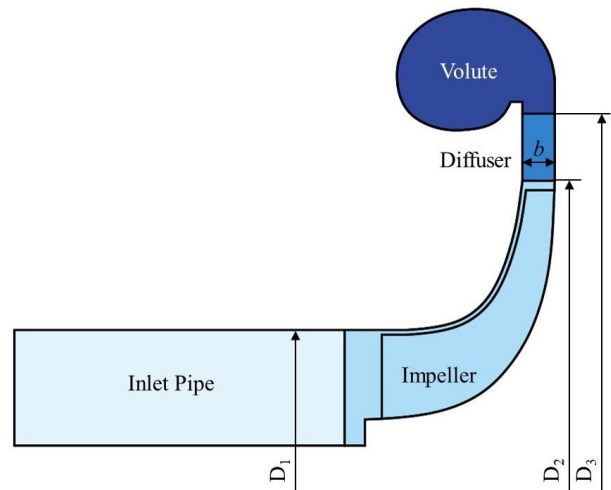


Fig. 1 Schematic diagram of the meridional cross-section

Table 1 Fundamental geometric characteristics of the centrifugal compressor

Geometric characteristics	Specific value
Main blades count	10
Splitter blades count	10
Diameter of impeller inlet D_1 /mm	34
Diameter of impeller outlet D_2 /mm	80
Diameter of volute inlet D_3 /mm	111
Width of diffuser b /mm	2.6
Tip clearance /mm	0.5

centrifugal compressor. The main components were an inlet tube, an impeller, a vaneless diffuser of parallel-wall design, and the volute. A schematic diagram of the meridional cross-section of the centrifugal compressor is illustrated in Fig. 1, and the fundamental geometric characteristics are provided in Table 1.

2.1 Numerical Methodology

The Fluent solver was utilized to carry out a steady-state numerical simulation of the compressible three-dimensional fluid dynamics within the compressor, which was achieved through the resolution of the RANS equations. Additionally, the closure was realized using the SST κ - ω turbulence model. The Coupled algorithm was used to accomplish coupling between the pressure and the velocity. The convective terms were discretized using a second-order upwind scheme, while the first-order upwind scheme was used to discretize the diffusion terms. The governing equations are as follows:

Continuity Equation (Engeda et al., 2003):

$$\frac{\partial}{\partial x_i}(\rho u_i) = 0 \tag{1}$$

where ρ is the density, with units of kg/m^3 , i represents the x , y , and z directions. u denotes the velocity with units of m/s .

The momentum equation is given by

$$\frac{\partial}{\partial x_i}(\rho u_i u_j) = -\frac{\partial p}{\partial x_i} + \frac{\partial \tau_{ij}}{\partial x_j} + \rho g_i + F_i \quad (2)$$

$$\tau_{ij} = \left[\mu \left(\frac{\partial u_i}{\partial x_j} + \frac{\partial u_j}{\partial x_i} \right) \right] - \frac{2}{3} \mu \frac{\partial u_i}{\partial x_i} \delta_{ij} \quad (3)$$

where μ represents the fluid dynamic viscosity, with units of Pa·s. g_i refers to the gravitational component vector in the i direction, with units of m/s^2 . p represents the pressure, with units of pa. F_i denotes the external force component. τ_{ij} is the stress tensor, given by Eq. (3).

Energy equation:

$$\frac{\partial}{\partial x_i}(\rho u_i T) = \frac{\partial}{\partial x_i} \left(\frac{\lambda}{c_p} grad T \right) + S_T \quad (4)$$

where T refers to the temperature, measured in K. c_p represents the specific heat capacity. λ is the thermal conductivity of the fluid, and S_T signifies the source term.

Many studies related to centrifugal compressors have utilized the SST $\kappa-\omega$ turbulence model (Xin et al., 2016; Raman & Kim, 2018), because it integrates the benefits of both the standard $\kappa-\omega$ and standard $\kappa-\epsilon$ models, using the $\kappa-\omega$ model to predict near-wall regions and the $\kappa-\epsilon$ model for other flow regions (Nili-Ahmadabadi et al., 2008). The equation for turbulence kinetic energy κ is given by (Li et al., 2024)

$$\frac{\partial(\rho k)}{\partial t} + \frac{\partial(\rho k u_i)}{\partial x_i} = \frac{\partial}{\partial x_j} \left(\Gamma_k \frac{\partial k}{\partial x_j} \right) + G_k - Y_k + S_k \quad (5)$$

The equation for the turbulence dissipation rate ω is as follows (Li et al., 2024):

$$\frac{\partial(\rho \omega)}{\partial t} + \frac{\partial(\rho \omega u_i)}{\partial x_i} = \frac{\partial}{\partial x_j} \left(\Gamma_\omega \frac{\partial \omega}{\partial x_j} \right) + G_\omega - Y_\omega + D_\omega + S_\omega \quad (6)$$

where G_k denotes the kinetic energy of turbulence, Y_k and Y_ω signify the turbulence dissipation for k and ω , respectively. D_ω refers to the term for convective diffusion. Γ_k and Γ_ω signify the effective diffusion coefficients, and S_k and S_ω correspond to the source terms.

2.2 Boundary Conditions

The boundary conditions needed to be specified during the solution of the governing equations. The pressure inlet was applied as the inlet boundary condition, with specified inlet total pressure and total temperature. The direction of the flow was normal to the inlet plane of the intake duct. The boundary condition at the outlet was set as the pressure outlet under high flow rate conditions, while the mass flow outlet condition was defined for the lower flow rate condition. The working medium was chosen as an ideal gas, and the adiabatic no-slip conditions were applied to the walls. The blades and the hub were treated as rotating walls with a predefined rotational speed and direction, while the other walls were set as stationary. The corresponding conditions for different boundaries are presented in Table 2. Convergence was achieved as the residuals reached 10^{-6} , which was assessed with the

Table 2 Boundary conditions with different operating conditions

Location	Boundary condition
Inlet of the computational domain	Pressure inlet
Wall of the blades and hub	Rotating wall
Other walls of the computational domain	Stationary wall
Outlet of the computational domain	Pressure outlet for high flow rate
	Velocity outlet for low flow rate

monitoring residuals, operating flow rate and outlet pressure. The computational domain of the centrifugal compressor was divided into rotating and stationary zones by employing the multiple reference frame (MRF) approach, which could solve the flow field involving rotating components. Among multiple domains, the individual zones could be set with the corresponding rotating speed, while the interfaces were used to separate the rotating zone and the stationary zone.

2.3 Establishment of Computational Mesh

The structured mesh for the impeller was generated using ANSYS TurboGrid, utilizing the ATM-optimized feature to enhance the single-passage topology, which was subsequently replicated rotationally to obtain a high-quality full-passage mesh for the impeller (Djodikusumo et al., 2016). Ten layers of mesh were applied to the impeller wall, the height of the first layer was specified as 0.007 mm. Considering the asymmetry geometry of the volute, the unstructured mesh was employed to construct a high-quality volute mesh. Additionally, an unstructured mesh was also acquired for the inlet pipe and the diffuser through ICEM. The computational domain of the centrifugal compressor is displayed in Fig. 2, and the mesh for the volute, diffuser, impeller, and inlet pipe is illustrated in Fig. 3.

To evaluate the influence of the mesh quantity on the simulation precision and optimize computational resources (Tian et al., 2021a), a mesh independence test was performed for the centrifugal compressor by establishing 10 groups of meshes for the computational

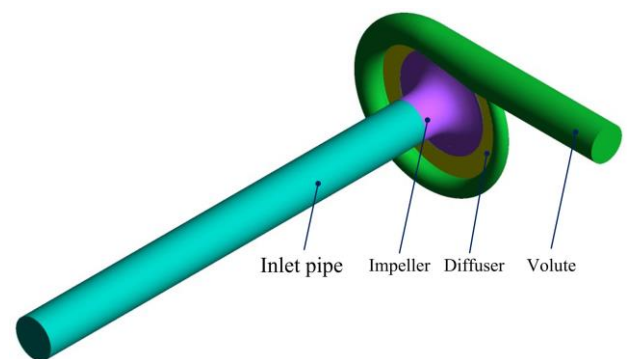


Fig. 2 Centrifugal compressor computational domain

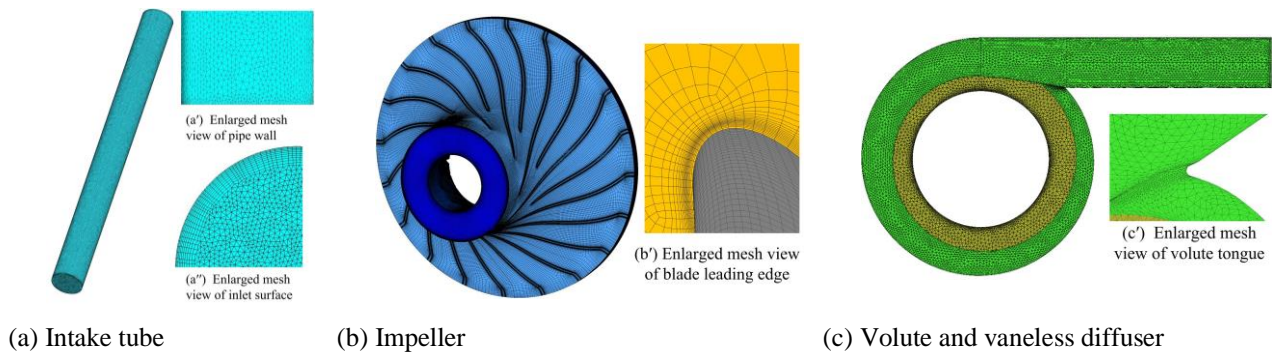


Fig. 3 Primary component meshes

Table 3 Ten groups of computational meshes

Mesh groups	Impeller	Volute	Inlet Pipe	Total mesh count
1	1,371,900	495,973	613,379	2,481,252
2	2,197,980			3,307,332
3	3,077,680			4,187,032
4	4,030,240			5,139,592
5	5,261,100			6,370,452
6	6,176,680			7,286,032
7	7,874,300			8,983,652
8	9,174,520			10,283,872
9	10,158,200			11,267,552
10	11,100,320			12,209,672

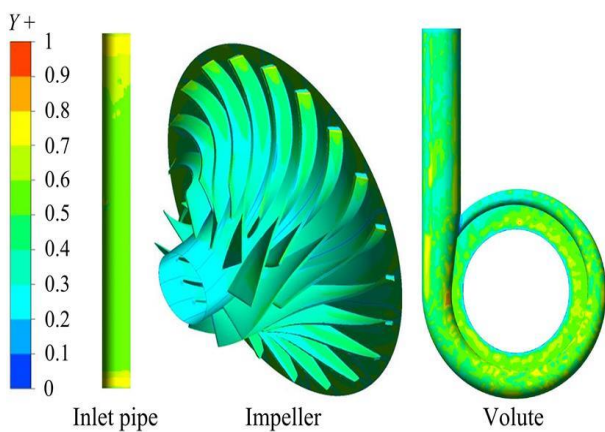


Fig. 4 Y+ distribution in different parts

domain. The number of 10 groups of meshes for different components of the centrifugal compressor is provided in Table 3. The overall mesh quality of the computational domain was above 0.4. The Y+ value for the inlet pipe, impeller, and volute for all mesh schemes was less than one in accordance with the specifications of the turbulence model. The Y+ distribution in different parts is reported in Fig. 4. With the premise of maintaining consistent prediction methodology, the predicted performance for the centrifugal compressor with various mesh schemes was evaluated under operating conditions of 0.043 kg/s and 6×10^4 rpm. The variations in

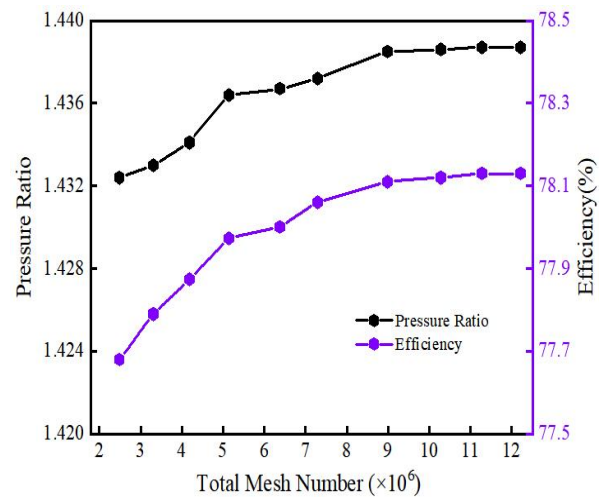


Fig. 5 Pressure ratio and efficiency variations

the performance parameters with the mesh quantity are depicted in Fig. 5. As illustrated in Fig. 5, the performance parameters remained essentially stable as the total count of meshes surpassed 8,983,652, which was selected for subsequent prediction. Additionally, the velocity variations of the selected lines in several sections of the intake pipe are depicted in Fig 6, while the chosen planes and the line of the intake pipes are marked in Fig. 7.

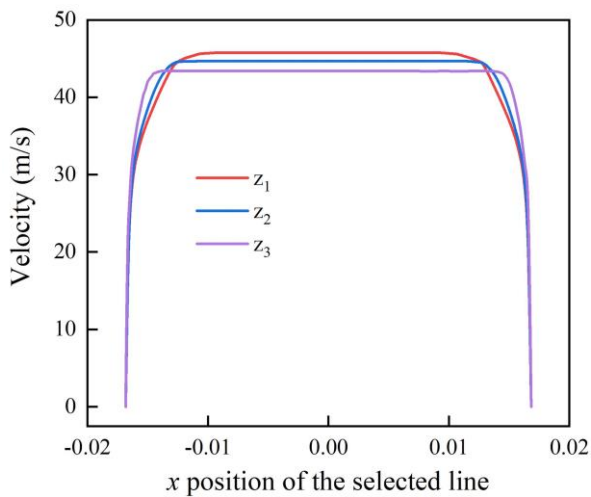


Fig. 6 Velocity profiles of selected lines

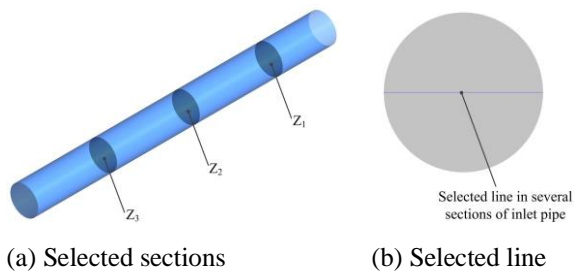
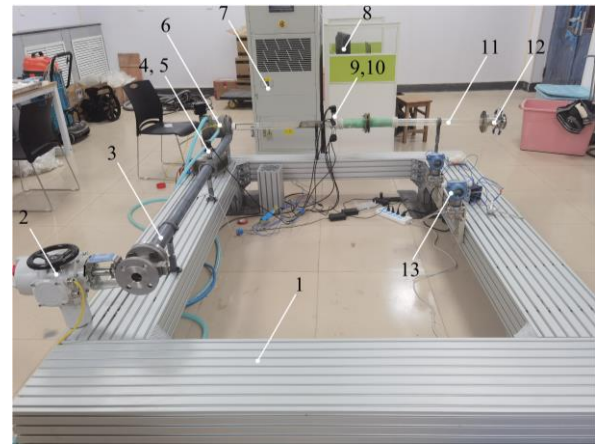


Fig. 7 Selected sections and line of intake pipe

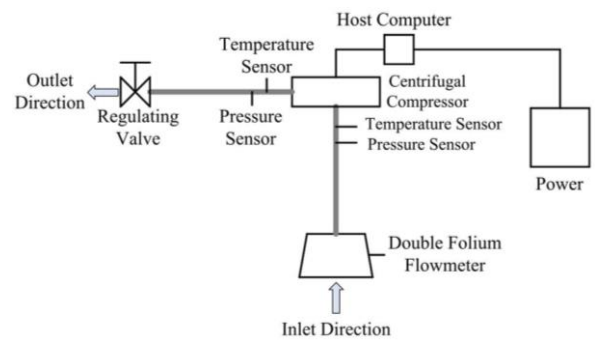
3. NUMERICAL PREDICTION OF THE CENTRIFUGAL COMPRESSOR CONNECTED TO INTAKE BENT DUCTS

3.1 Numerical Methodology Validation

To achieve the validation of the computational methodology, the performance behavior of the centrifugal compressor connected to a rectilinear intake tube with rotating speeds of 6×10^4 , 8×10^4 , and 10×10^4 rpm was experimentally tested. The Reynolds number range considered for various rotational speeds and operating flow rate condition was approximately 7×10^4 – 22×10^4 . The arrangement and the schematic diagram of the performance test rig are depicted in Fig. 8(a) and (b). The essential testing parameters included the operating mass flow rate, rotational speed, pressure, and temperature at the inlet and outlet pipes. The experimental setup was powered by an electrical supply, and the centrifugal compressor's operating rotational speed was governed through a PLC-based program on a host computer. A regulating valve was mounted to regulate the outlet pressure, and the operating flow rate of the fluid was gauged using a double folium flowmeter when the compressor operated steadily, while the pressure and temperature data were recorded with sensors configured at the inlet and outlet pipes. The main testing parameters were finally collected for various operating conditions by regulating the outlet pressure and operating rotational speed, which were averaged over a stable operating



(a) Performance test rig arrangement. (1) Test rig foundation; (2) Regulating valve; (3) Outlet pipe; (4) Pressure sensor of outlet pipe; (5) Temperature sensor of outlet pipe; (6) Centrifugal compressor; (7) Electrical supply; (8) Host computer; (9) Pressure sensor of inlet pipe; (10) Temperature sensor of inlet pipe; (11) Inlet pipe; (12) Double folium flowmeter; (13) Difference pressure transmitter



(b) Schematic diagram of the performance test rig

Fig. 8 Performance test rig for the centrifugal compressor

period of 5 min. A total of three repetitions were conducted for each experiment to ensure consistency. Error bars representing the standard deviations of the experimental results are depicted in Fig. 9.

The testing parameters for each rotational speed condition were obtained by gradually adjusting the operating condition. The operating performance parameters of the centrifugal compressor were derived by incorporating the measured pressure and temperature into the performance calculation equations.

Figure 9 presents the pressure ratio and efficiency variations at various rotational speeds, as obtained from both the experimental measurements and the numerical predictions. The calculations for determining the pressure ratio and efficiency are outlined below:

$$\pi_c = \frac{P_{out}}{P_{in}} \quad (7)$$

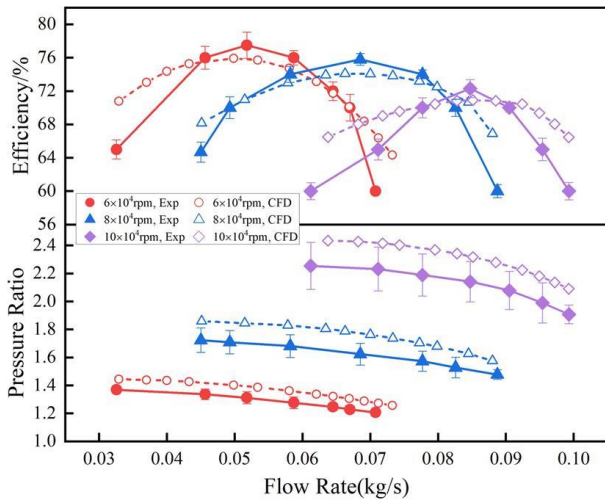


Fig. 9 Performance variations of centrifugal compressor

$$\eta = \frac{T_{in} (\pi_c^{\frac{k-1}{k}} - 1)}{T_{out} - T_{in}} = \frac{\pi_c^{\frac{k-1}{k}} - 1}{\frac{T_{out}}{T_{in}} - 1} \quad (8)$$

where P_{in} and P_{out} represent the total pressure, while T_{in} and T_{out} represent the total temperatures of the inlet and outlet pipes, respectively. k denotes the isentropic coefficient, with a value of 1.4.

As shown in Fig. 9, the performance variations derived from both the numerical simulations and the experimental measurements demonstrated a consistent trend across all rotational speed conditions, with the differences remaining within 10%. The discrepancies between the experimental and predicted outcomes were primarily attributed to factors such as manufacturing precision deviations and heat loss due to cooling water during the experiments. These conditions differed from the adiabatic wall conditions assumed in the simulation process (Tian et al. 2021b). In addition, the secondary effects in the simulation due to the flow regime in the compressor might have contributed to this deviation. Despite these differences, the numerical results effectively predicted the range of stable operation and the corresponding optimal efficiency operating condition of the centrifugal compressor, indicating a high degree of reliability and accuracy for the simulation approach (Tian et al., 2021b). Consequently, the simulation method was employed in the subsequent research to investigate the flow behavior and operating performance of the centrifugal compressor.

3.2 Numerical Simulation of Centrifugal Compressor connected to Curved Ducts

In practical applications, the intake pipeline of a centrifugal compressor is customarily a curved duct due to spatial constraints, resulting in the alteration in the airflow direction within the curved intake ducts. To explore the effect of various curved intake ducts on the centrifugal compressor’s operating performance, four structures for intake bent pipes were established, i.e., P_c , P_{c-o} , P_{nc} , and P_{nc-o} , while the first part of P_{c-o} and P_{nc-o} were

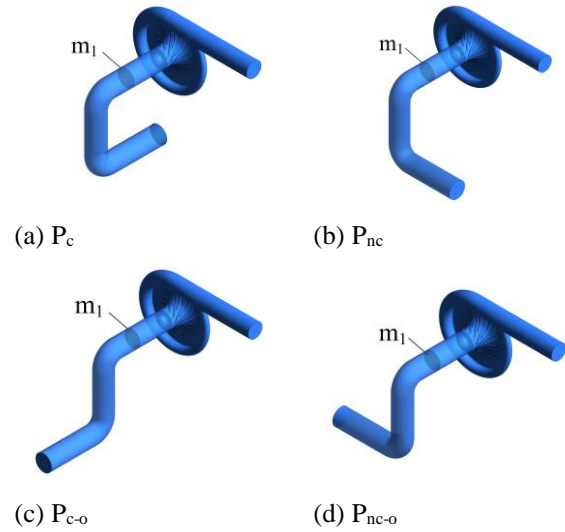


Fig. 10 Centrifugal compressor computational domain connected to various curved intake tubes

in the opposite direction to P_c and P_{nc} , respectively. Additionally, centrifugal compressor’s performance behavior connected to a rectilinear intake tube (P_s) was numerically simulated for comparison. The lengths along the central axis for P_s , P_c , P_{c-o} , P_{nc} , and P_{nc-o} were kept identical at 360 mm, ensuring consistent linear loss in the ducts, so the variations in the compressor’s performance were attributed to the differences in the intake pipe structures. The centrifugal compressor computational domains connected to various curved intake tubes are depicted in Fig. 10.

The variations in the operating performance behavior with various intake bent ducts were obtained by altering the boundary conditions. The simulations were conducted for three rotational speeds: 6×10^4 rpm, 8×10^4 rpm, and 10×10^4 rpm. The predicted performance is shown in Fig. 11. The forecasted results demonstrated that the performance parameters of the centrifugal compressor connected to P_c , P_{c-o} , P_{nc} , and P_{nc-o} were continuously lower than those with P_s , indicating that the installation of the intake bent ducts induced a certain degree of performance degradation. Moreover, the extent of reduction in efficiency and pressure ratio became more pronounced with the increment of the rotational velocity and mass flux. In addition, the simulated results indicated that the performance behavior between P_c and P_{c-o} as well as P_{nc} and P_{nc-o} showed a consistent variation trend under various rotational speed conditions, and the performance discrepancy between P_c and P_{c-o} as well as P_{nc} and P_{nc-o} was relatively small. Among all rotational velocity scenarios, the centrifugal compressor’s operating performance characteristics associated with P_{nc} and P_{nc-o} was consistently lower than that with P_c and P_{c-o} , which revealed that the extent of performance degradation varied with the intake pipe structure. Although the dimensions along the central axis of the four intake bent pipes were identical, P_{nc} and P_{nc-o} exerted a more substantial influence on the performance compared to P_c and P_{c-o} .

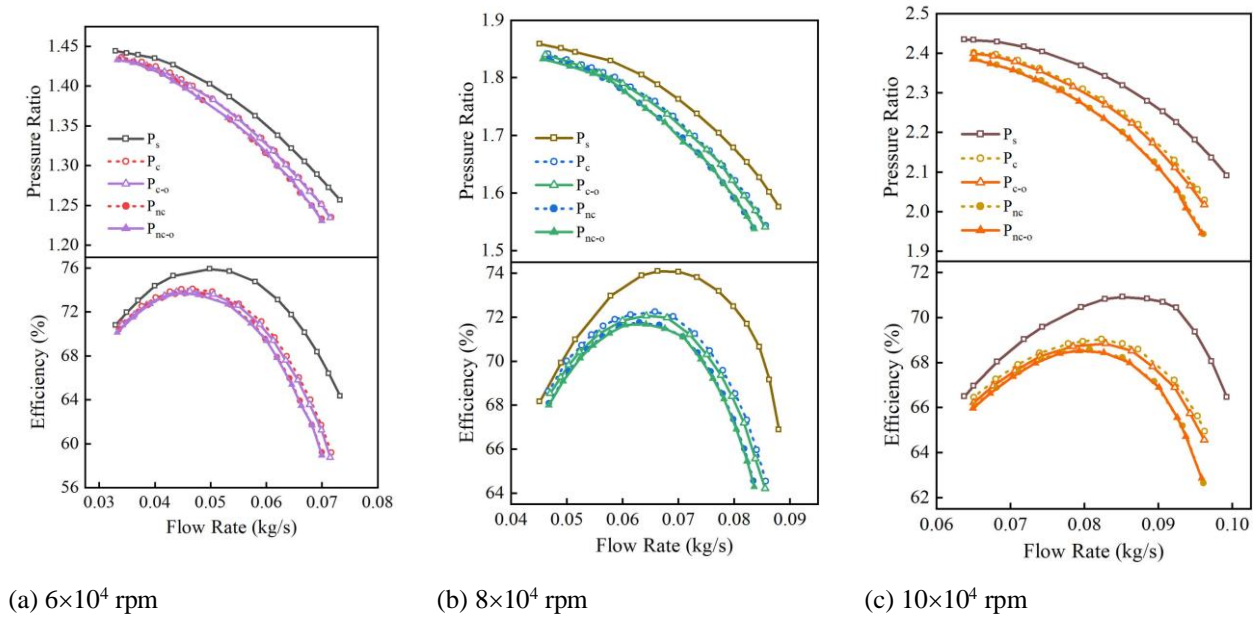


Fig. 11 Performance variations with different inlet pipes

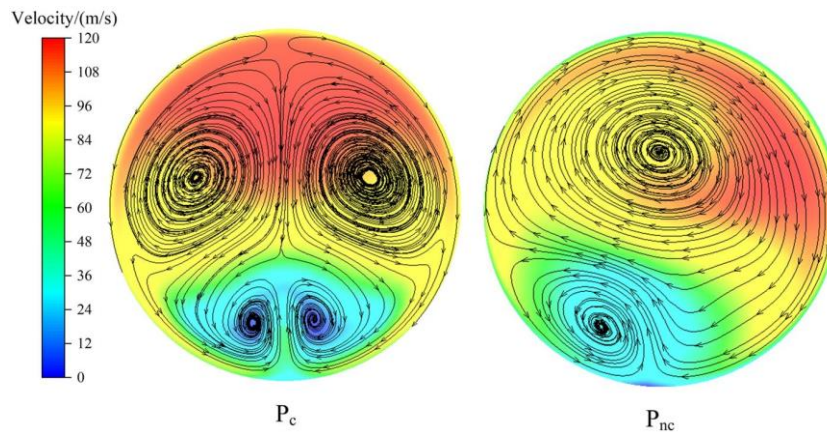


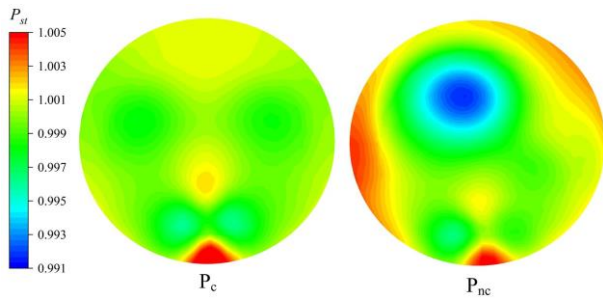
Fig. 12 Streamline distribution for different inlet pipes

To analyze the discrepancy in performance caused by different intake pipelines, it was essential to evaluate the flow dynamics at intake pipelines outlet. Considering the consistent performance variation trend of the centrifugal compressor between P_c and P_{c-o} as well as P_{nc} and P_{nc-o} , and the similar structural features, the inlet bent pipe structures of P_c and P_{nc} were selected for the subsequent analysis. The flow field distribution at section m_1 of P_c and P_{nc} was selected for analysis, while the flow characteristics maintained the swirling distribution as it flowed out through the elbow. This section was positioned 100 mm upstream of the impeller inlet, as marked in Fig. 10.

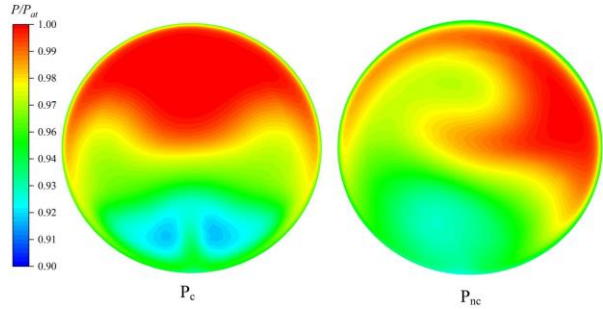
Figure 12 illustrates the distribution of streamlines for P_c and P_{nc} at high-efficiency conditions for the operating rotational velocity of 10×10^4 rpm, with flow rates of 0.08513 kg/s and 0.08515 kg/s. As demonstrated in Fig. 12, a symmetrical swirling distribution was generated at the outlet section of P_c , while an offset swirling flow distribution was present at section m_1 of P_{nc} , with the main swirling rotating in a clockwise direction

when viewed from the impeller inlet. This was consistent with the impeller's rotation direction. Based on the flow distribution observed at the bent pipes outlet, it was evident that the high-speed regions of distorted flow with P_c and P_{nc} were both located in the upper axial area of the pipes, corresponding to the main swirling zone, whereas the low-velocity regions were positioned in the lower axial area of pipes. Although the flow field distribution for the case P_c and P_{nc} usually exhibited unsteadiness and periodicity over time, the swirling distribution pattern at the outlet section of intake bent ducts remained basically similar, staying unchanged with the alteration of the operating flow rate conditions. Additionally, the primary purpose of the investigation was to quantify the correlation between the performance deterioration extent and the distortion degree of the flow characteristics within the curved intake tubes, therefore the steady-state simulation results could fulfill this research purpose.

The dimensionless static pressure (P_{st}) distribution at section m_1 for the two intake bends is illustrated in Fig. 13(a), while the variation of the non-dimensional total



(a) Dimensionless static pressure distribution



(b) Dimensionless total pressure distribution

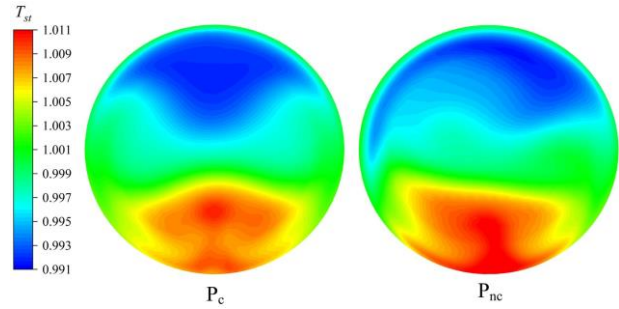
Fig. 13 Dimensionless pressure distribution of different inlet pipes

pressure at section m_1 for the two intake bends is depicted in Fig. 13(b). This parameter was defined as the total pressure at a specific location divided by the atmospheric pressure P_{at} , with the value of 101,325 Pa. Figure 13 demonstrated that the non-dimensional total pressure at P_c and P_{nc} outlet section exhibited a similar distribution to the velocity. The regions with higher velocity in the pipes corresponded to the higher total pressure area, which was the upper axial region. Consequently, the main swirling regions of both P_c and P_{nc} were characterized by high total pressure and velocity. As the fluid flowed through the bend, the flow velocity within the outer side of the bend increased, while the velocity near the inner wall decreased, leading to the increase in dynamic pressure within the outer region of the curved duct. Although the static pressure within the high-velocity area of the chosen section was slightly reduced, the presence of swirling flow within the bent pipe led to an increment in the dynamic pressure near the outer region. Consequently, the total pressure in this region increased. The average total pressure in section m_1 and section m_2 are presented in Table 4. Section m_2 was positioned 10 mm upstream from the entrance of the impeller. The variation in the mean total pressure indicated that the total energy at the outlet of P_{nc} in different sections was lower than that of P_c , meaning that the flow loss within P_{nc} was higher, while the total energy of section m_2 for P_c and P_{nc} was partially restored compared to that of section m_1 .

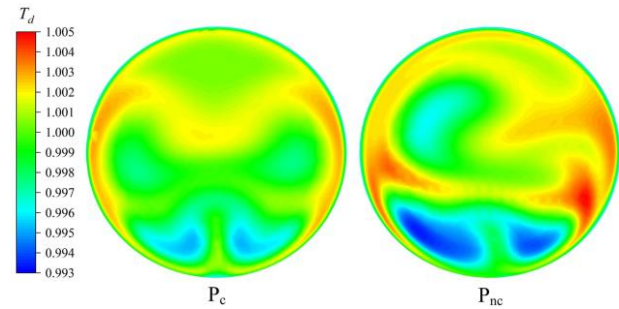
The non-dimensional static temperature (T_{st}) distribution and the total temperature (T_d) at section m_1 with different intake bent pipes are shown in Fig. 14. This temperature was defined as the local temperature divided by the mean temperature of section m_1 . It can be seen that the distributions of T_{st} and T_d with P_c and P_{nc} were different, while the distributions of T_{st} and T_d of P_c both

Table 4 Average total pressure in sections m_1 and m_2

Inlet pipes	Section	Average total pressure/Pa
P_c	m_1	98327
	m_2	98719
P_{nc}	m_1	98022
	m_2	98413



(a) Dimensionless static temperature distribution



(b) Dimensionless total temperature distribution

Fig. 14 Dimensionless temperature distribution for different inlet pipes

exhibited a symmetric distribution trend in section m_1 . In the upper axial area of the section with high total pressure and velocity, the static temperature was relatively low, while the total temperature was higher. Within section m_1 , the static temperature and the total temperature distribution with the P_{nc} configuration were more uneven, with a larger temperature gradient. Considering the efficiency calculation for the centrifugal compressor, the augmentation of total temperature resulted in a decline in the operational efficiency because the fluid kinetic energy was partially converted into internal energy. Therefore, the centrifugal compressor connected to P_{nc} exhibited lower efficiency compared to P_c .

3.3 Quantitative Characterization of the Distorted Flow Field Across Various Intake Bent Ducts

From the streamline distribution at the outlet of the intake bends, it could be observed that the swirling flow structure was formed as the fluid passed through the curved pipe. Furthermore, the flow pattern and the swirling intensity at the outlet of the elbows varied with the structure of the curved pipelines. Additionally, Fig. 13 illustrates the fact that the distorted distribution of the non-dimensional total pressure was observed at the intake bent ducts outlet section, primarily manifesting as

circumferential distortion (Zhou & Wen, 2005). To quantify the effect of the entrance pipelines on the outlet flow characteristics and establish the correlation with the variations in the operating performance behavior, it was essential to quantitatively characterize the distorted flow within the pipelines outlet. Therefore, the swirling intensity (*SI*) was employed to characterize the intensity of the swirling distortion at the outlet of the bends (Xu et al., 2017). The value of *SI* was always positive, with a higher value indicating a greater swirling distortion extent of the flow field. The distorted total pressure at the bend outlet was quantitatively described with the circumferential distortion degree (*CD*) (Xu et al., 2018), indicating the decrease extent in the total pressure within a specific circular area of section m_1 . The swirling intensity at a specific radius is defined as follows:

$$SI_i = \frac{SS_i^+ \times \theta_i^+ + |SS_i^-| \times \theta_i^-}{360} \quad (9)$$

where SS_i^+ and SS_i^- represent the average areas of the swirling regions along the positive and negative directions, respectively, which can be derived using the following equations:

$$SS_i^+ = \frac{1}{\theta_i^+} \int_{\theta_i^+} \alpha(\theta)_i d\theta \quad (10)$$

$$SS_i^- = \frac{1}{\theta_i^-} \int_{\theta_i^-} \alpha(\theta)_i d\theta \quad (11)$$

where θ_i^+ and θ_i^- denote the circumferential ranges for the positive and negative swirling angles, respectively, while $\alpha(\theta)_i$ is the fitting function for the positive and negative swirling angles at different circumferential regions. The swirling angle α is defined as follows:

$$\alpha = \arctan\left(\frac{U_\theta}{U_x}\right) \quad (12)$$

where U_θ represents the local circumferential velocity at the outlet section with a specific radius, and U_x represents the axial velocity. A positive α indicates that the swirling direction is consistent with the impeller's rotation direction, whereas a negative α signifies the direction opposite to the impeller rotation orientation.

The calculation for the circumferential distortion extent is:

$$CD = \frac{(P_m)_i - (P_{m-low})_i}{(P_m)_i} \quad (13)$$

where $(P_m)_i$ refers to the mean value of the total pressure within a specific circular area, and $(P_{m-low})_i$ denotes the average value of the total pressure which is lower than $(P_m)_i$ within the same radial area.

Figure 15 illustrates nine circumferential circles at section m_1 , ranging from 10% to 90% of R , with R denoting the semidiameter of the intake tube. The variations in *SI* and *CD* under various flow rate conditions of P_c and P_{nc} are shown in Fig. 16. The operating rotating speed was 10×10^4 rpm, and the flow rates were 0.08513

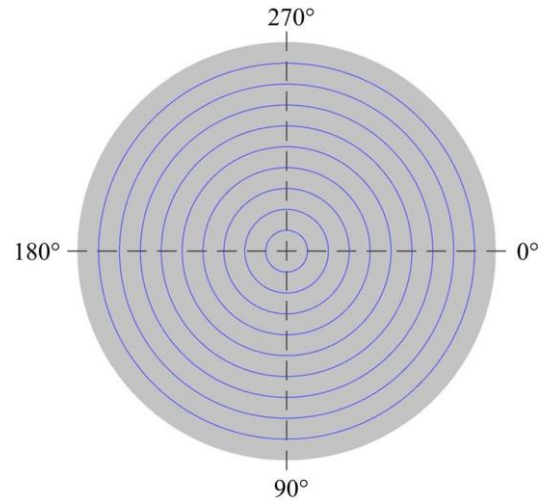
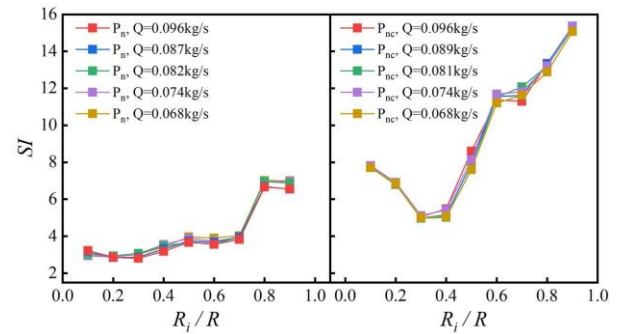
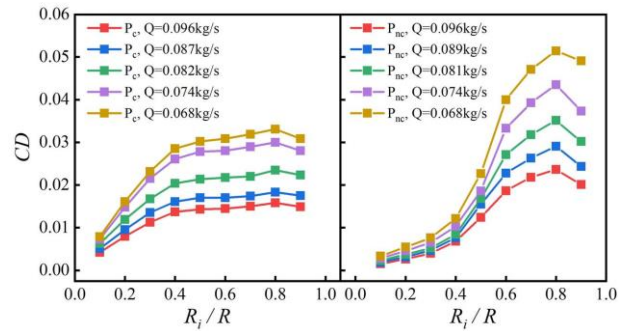


Fig. 15 Schematic diagram of nine circumferential circles in section m_1



(a) Variations in swirling intensity

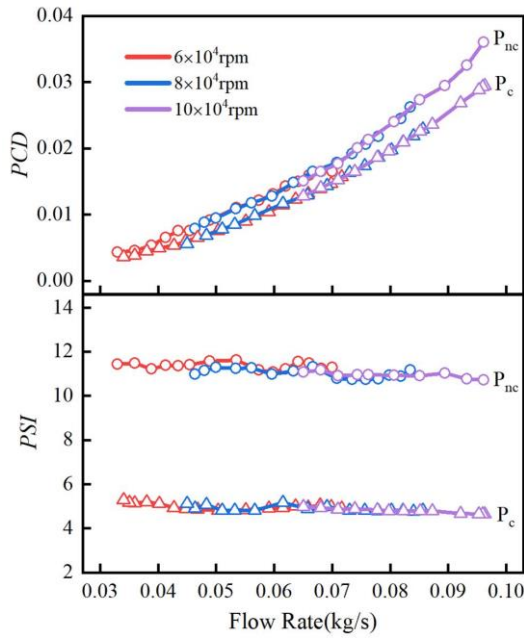


(b) Variations in circumferential distortion degree

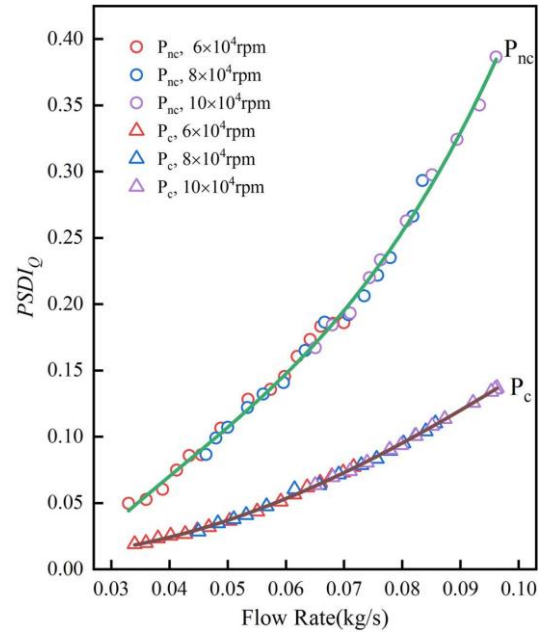
Fig. 16 Variations in distortion extent at the intake pipelines outlet

and 0.08515 kg/s. The horizontal coordinate represents the dimensionless radius of section m_1 , determined by the ratio of the specific local radius to R .

As depicted in Fig. 16, the *SI* of P_c was generally lower compared to that of P_{nc} under each rotational velocity condition, its increase rate with the radius was relatively small. The *SI* of P_{nc} was higher than that of P_c at each corresponding radius, indicating a more intense distorted swirling flow dynamics at the P_{nc} outlet. The range of the area with the high swirling intensity of P_{nc} was broader than that of P_c , and the *SI* of P_{nc} increased



(a) Variations of *PSI* and *PCD*



(b) Variations of *PSDI*

Fig. 17 Variations of distortion intensity across various operating scenarios

more significantly along the radial direction in the high radius region. Additionally, Fig. 16 shows that the *SI* of P_c and P_{nc} exhibited subtle variations across different flow rate conditions. The *SI* remained nearly consistent at the corresponding radius, which indicated that the variations of the flow rate exerted a negligible effect on the swirling intensity of the intake pipes. Consequently, the primary factor affecting the swirling intensity was the structure of the intake bends, rather than the operating flow rate conditions. The *CD* of P_c and P_{nc} demonstrated an overall growing trend with the radius, indicating a greater reduction degree in the total pressure in the higher radius region. However, there were notable differences in *CD* between P_c and P_{nc} , and the increasing trend of *CD* with P_{nc} was more significant within the high radius region compared to P_c . Under various flow rate conditions, the *CD* of both intake elbows increased with increasing flow rate, while the maximum *CD* of P_{nc} was consistently higher compared to P_c at all rotational speed conditions. The variation in *CD* across various flow rate conditions revealed that the increment of the flow rate led to greater circumferential distortion degree in total pressure within the curved inlet tube. The inlet bends geometric construction influenced the maximum value of *CD*. Specifically, P_{nc} generated the flow field possessed a higher distortion degree of circumferential total pressure compared to P_c . Due to the differences in the swirling distortion extent and the circumferential distortion degree in total pressure for P_c and P_{nc} , the contributions on the centrifugal compressor’s operating behavior differed as well.

The swirling intensity of the plane (*PSI*) and the circumferential distortion of the plane (*PCD*) are introduced to quantify the distortion extent of the flow within curved pipeline, i.e., section m_1 . Additionally, the plane superimposed distortion intensity (*PSDI*) is

employed to quantitatively characterize the combined intensity of the uneven flow. The relevant calculations are as follows:

$$PCD = \frac{\sum_{i=1}^N R_i CD_i}{N} \quad (14)$$

$$PSI = \frac{\sum_{i=1}^N R_i SI_i}{N} \quad (15)$$

$$PSDI_Q = PCD_Q \cdot PSI_Q \quad (16)$$

where the value of N is 9, R_i represents the radius of each circumference within section m_1 , CD_i signifies the extent of circumferential distortion, and SI_i is the swirling intensity at a specific radius. The subscript Q refers to the operating flow rate. Figure 17 illustrates the variations of *PSI*, *PCD*, and *PSDI* under different flow rate conditions at the rotational speeds of 6×10^4 , 8×10^4 , and 10×10^4 rpm. As illustrated in the figure that the *PCDs* for both inlet elbows showed an increasing trend for all rotational speed conditions with the same growth rate, and the value of *PCD* was consistently higher than that of P_c as the flow rate varied. The *PSI* of both intake elbows remained nearly unchanged as the flow rate grows, while the *PSI* of P_{nc} was greater at each flow rate condition, being approximately twice that of P_c . As shown in Fig. 17, the *PSDI*s of P_c and P_{nc} exhibited an upward trend as the flow rate increased across various rotational speed conditions, with the growth following a relatively consistent trend. Moreover, the *PSDI* of P_{nc} was higher and presented a greater growth trend compared to that of P_c at each flow rate condition. At the operating condition with a high rotational velocity and a large mass flux, the maximum *PSDI*s for P_c and P_{nc} reached 0.137 and 0.386,

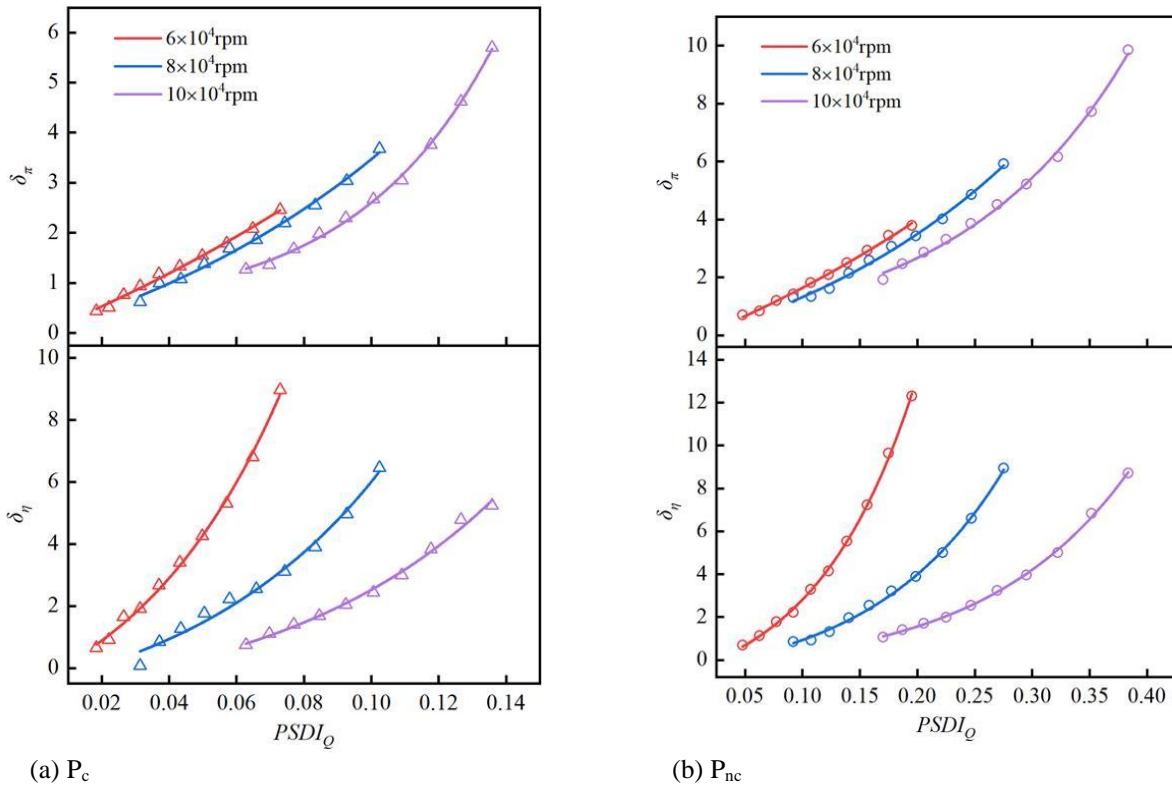


Fig. 18 Variations of the performance degradation degree

respectively. Based on an analysis of the performance variations with different intake pipes, it could be concluded that the greater distortion intensity within the bends resulted in a more significant deterioration extent for the performance.

In order to quantitatively determine the correlation between the superimposed distortion intensity of the plane and the performance characteristics, several identical flow rates were selected for both P_c and P_{nc} across multiple rotational velocity scenarios, and the corresponding $PSDI$ and the performance parameters were extracted. The performance degradation degree was employed to quantify the reduction extent in the operating performance when the system connected to bent pipes relative to the straight intake tube.

$$\delta_\pi = \frac{\pi_i - \pi_s}{\pi_s} \tag{17}$$

$$\delta_\eta = \frac{\eta_i - \eta_s}{\eta_s} \tag{18}$$

where δ signifies the performance degradation degree, π and η represent the pressure ratio and efficiency. The subscript i denotes the corresponding performance parameters related to P_c and P_{nc} , respectively, while subscript s refers to those with P_s . Figure 18 illustrates the variation of the performance degradation extent for different flow rate and rotational velocity conditions with the superimposed distortion intensity of the plane. The relationships between δ_π , δ_η , and $PSDI$ for both P_c and P_{nc} were fitted using exponential functions. The fitting function is as follows:

$$\delta = a + b \cdot e^{c \cdot PSDI} \tag{19}$$

where δ is the deterioration extent of the performance parameters, including the pressure ratio decline extent δ_π and the efficiency decline extent δ_η . a , b , and c refer to the coefficients of the exponential functions, and the values for different rotational speed conditions are presented in Table 5.

As shown in Fig. 18, the δ_π and δ_η for the centrifugal compressor with P_c and P_{nc} increased as the $PSDI$ rose, since the value of $PSDI$ with P_{nc} was higher compared to P_c across all operating rotational velocity conditions, and the deterioration extent of the performance associated with P_{nc} was consequently greater compared to that associated with P_c . Structural differences in the intake pipes resulted in variations in the flow distortion intensity at the discharge section of the bent pipelines, inducing varying reduction extent in the performance parameters. However, the increasing trend in the distortion intensity consistently contributed to a greater decline extent of the compressor's performance. At identical flow rate conditions across various rotational speeds, the operating performance parameters associated with P_{nc} exhibited a greater deterioration degree than the P_c scheme. The maximum reduction degrees for the pressure ratio for P_c and P_{nc} were approximately 5.7% and 9.8%, respectively, under high rotational speed conditions, while the maximum degradation degrees for the efficiency were approximately 5.3% and 8.7%, respectively. The quantitative correlation between the superimposed distortion intensity of the plane and the performance degradation extent could contribute valuable insights for predicting the operating performance when adopting intake curved pipelines.

Table 5.1 Exponential function Coefficients (δ_π and $PSDI$)

Inlet pipe	Rotational speed (rpm)	a	b	c	Adjusted R-Square
P_{nc}	6×10^4	-6.82	6.62	2.45	0.996
	8×10^4	-2.86	2.75	4.20	0.994
	10×10^4	-0.17	0.73	6.80	0.996
P_c	6×10^4	-5.00	4.94	5.63	0.994
	8×10^4	-2.06	2.05	9.93	0.992
	10×10^4	0.38	0.20	24.26	0.998

Table 5.2 Exponential function Coefficients (δ_η and $PSDI$)

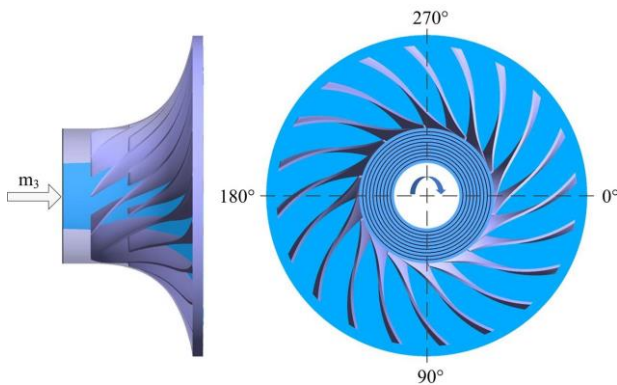
Inlet pipe	Rotational speed (rpm)	a	b	c	Adjusted R-Square
P_{nc}	6×10^4	-2.09	1.57	11.39	0.999
	8×10^4	-1.27	0.93	8.70	0.997
	10×10^4	-0.61	0.45	7.95	0.998
P_c	6×10^4	-2.88	2.46	21.42	0.997
	8×10^4	-2.03	1.53	16.60	0.986

4. FLOW FIELD DISCUSSION WITHIN THE IMPELLER

The impeller serves as the dominant working part of the centrifugal compressor, the flow characteristics within it is intrinsically related to the performance. To assess the influence of the inlet pipes on the flow dynamics at the impeller inlet, it is essential to extract and analyze the flow field within impeller while adopting different intake bent pipes. The section m_3 at impeller entry zone was selected, as marked in Fig. 19(a). Nine circumferences were chosen in section m_3 , corresponding to 0.1–0.9 times the blade height, as illustrated in Fig. 19(b). In addition, the impeller rotated along the clockwise direction when viewed from the inlet. To clearly depict the variation in the flow field across various blade heights for the impeller along the theta direction, the distribution of the non-dimensional total pressure at various blade heights for P_c and P_{nc} was extracted, with the rotational velocity of 10×10^4 rpm, and the operating flow rate conditions of $Q=0.08513$ kg/s and $Q=0.08515$ kg/s. The findings are presented in Fig. 20.

As demonstrated in Fig. 20, the intake elbows affected the distribution of the non-dimensional total pressure within section m_3 , and the variation region of the total pressure within section m_3 closely corresponded to the uneven total pressure region within the intake elbows outlet section. The regions with higher total pressure at the discharge section of the curved intake ducts resulted in the region with higher total pressure at the impeller entry section. The lower total pressure region of P_c was within the circumferential angle range of 36° – 144° , while the higher total pressure region spanned from 216° to 324° . P_{nc} possessed a wider low-pressure region, primarily between 72° and 252° , with a reduced high-pressure region. The distribution range of the low-pressure region at different blade heights for P_{nc} was more extensive, indicating a significant total pressure reduction extent along the theta direction. As a result, P_{nc} presented a higher distortion extent in total pressure at the impeller entry section. This observation implied that the flow distribution with offset swirling at the discharge section of the curved intake duct contributed to a more significant uneven flow degree at the impeller entrance.

Figure 21 illustrates the changes in mass flow rate along the theta direction, as well as the axial velocity fluctuations at various blade heights on section m_3 , which were both dimensionless values and defined as the ratio of the local mass flow rate or the axial velocity to the average value within the corresponding region. As observed in Fig. 21, there was a direct correlation between the axial velocity and the mass flow rate. The flow at the impeller entrance region with lower total pressure exhibited a reduced axial velocity, resulting in a decreased mass flow entering the corresponding flow passage. The variation of the mass flow rate presented a comparable trend to the change of axial velocity. Since the total pressure reduction within the lower total pressure region at the impeller entrance section for P_{nc} was greater than that of P_c , the axial velocity at the corresponding area was lower as well, leading to a relatively smaller mass



(a) Selected section (b) Nine circumferences
Fig. 19 Selected section and circumferences

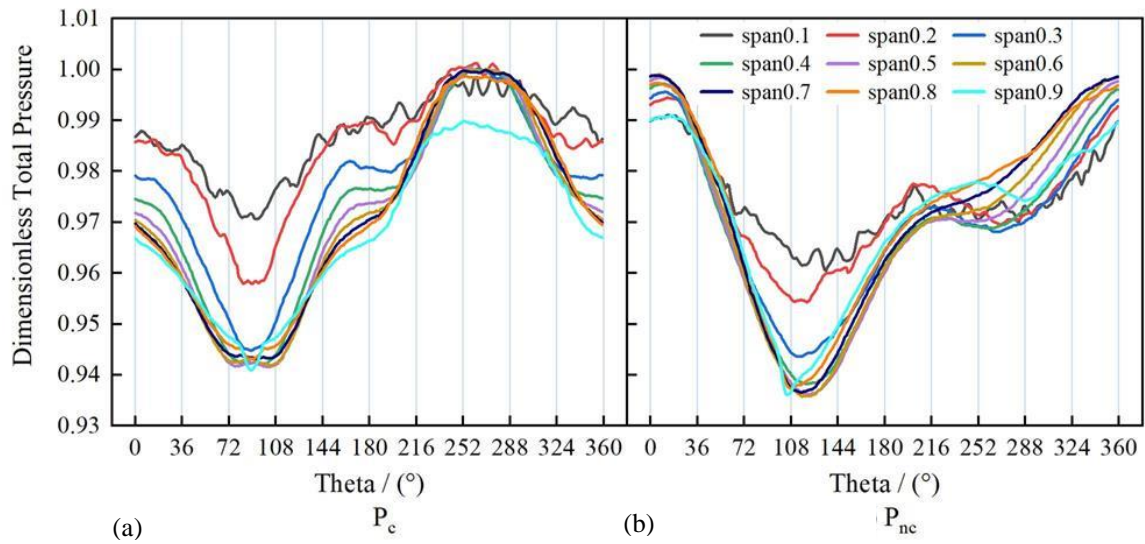


Fig. 20 Non-dimensional total pressure distribution along the theta direction

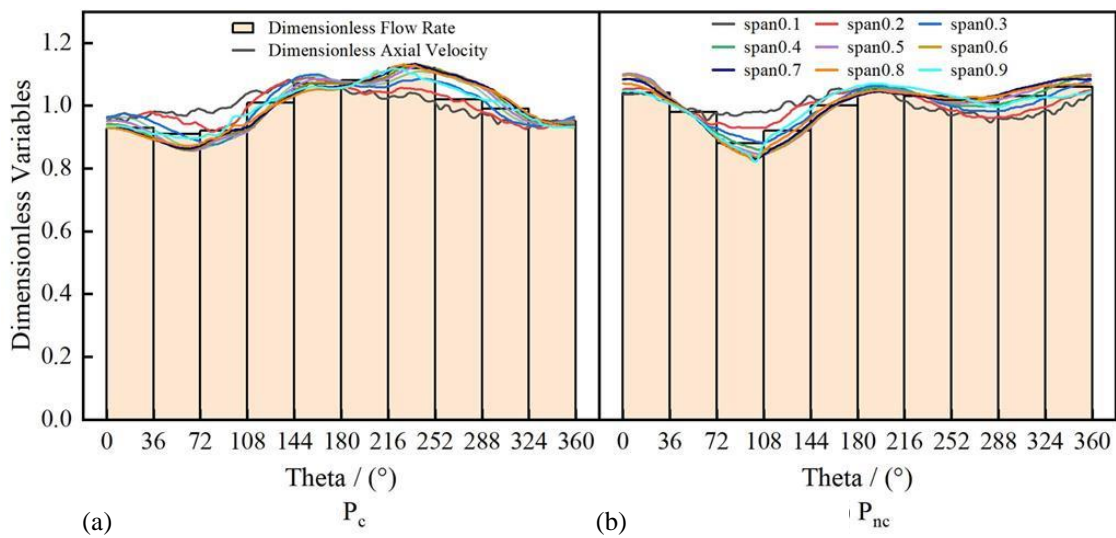


Fig. 21 Variations of the mass flow rate and axial velocity

flow entering the flow passage in these circumferential areas. The distorted flow associated with the total pressure and swirling distribution at the discharge section of the intake duct caused an uneven spread of the mass flow rate within the impeller passage. Furthermore, this non-uniformity adversely affected both the pressurization capability of the impeller and the stability of the flow behavior, ultimately causing the deterioration in the performance characteristics.

Figure 22 demonstrates the variation of the circumferential velocity across various span locations at the impeller entry section. The results in Fig.22 exhibited that as the blade height increased, the circumferential velocity of the fluid became greater for both P_c and P_{nc} , while the magnitude of the circumferential velocity with P_{nc} was lower than that of P_c at each corresponding span location. This implied that less energy was contained by the fluid with the adoption of P_{nc} . The reduction region of the circumferential velocity maintained the similarity with the variation of the axial velocity, and the decrease

degree in both velocities with P_{nc} was more pronounced, indicating that P_{nc} exerted a greater impact on the energy of the fluid at the impeller inlet. This further affected the flow within the downstream passage.

The magnitude of the turbulent kinetic energy reflected the stability of the flow. Therefore, it was necessary to extract and examine the distribution of the turbulent kinetic energy within the impeller passages. According to relevant literature references, the turbulent kinetic energy characterizes the intensity of the turbulence, and its magnitude is proportional to the velocity fluctuations. Higher turbulent kinetic energy indicates a more disordered flow, which implies greater flow losses in the corresponding region (Cheng et al., 2019; Jiang & Zhu, 2022). Figure 23(a) and (b) illustrates the turbulence kinetic energy within sections m_1 and m_2 of the intake pipes, and the average turbulence kinetic energy is reported in Table 6. As depicted in Fig. 23, the higher turbulence kinetic energy area for different sections of P_c showed consistent distribution

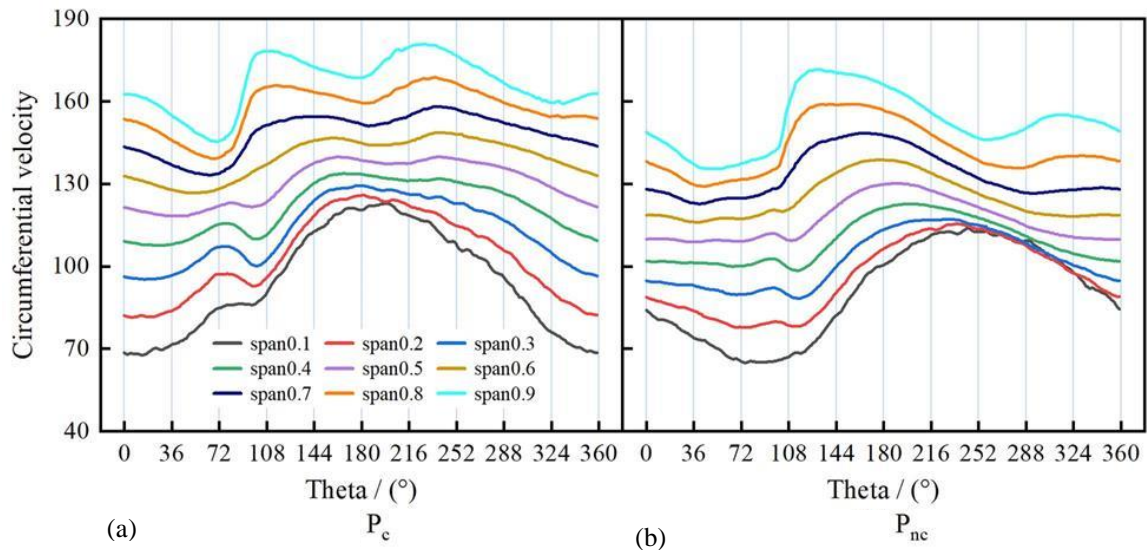
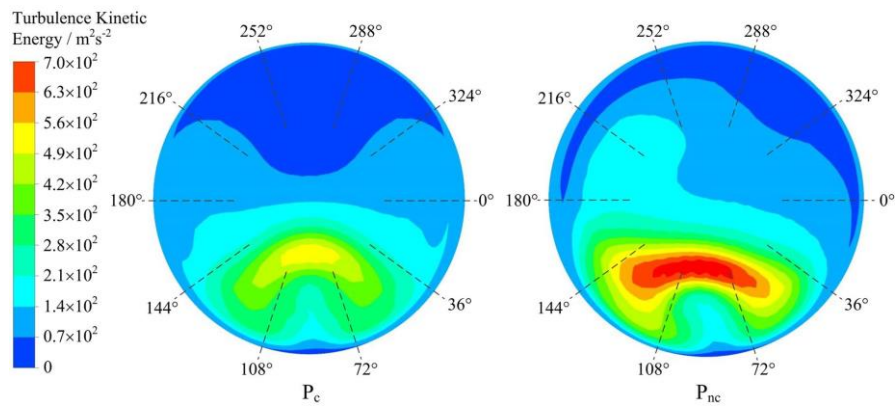


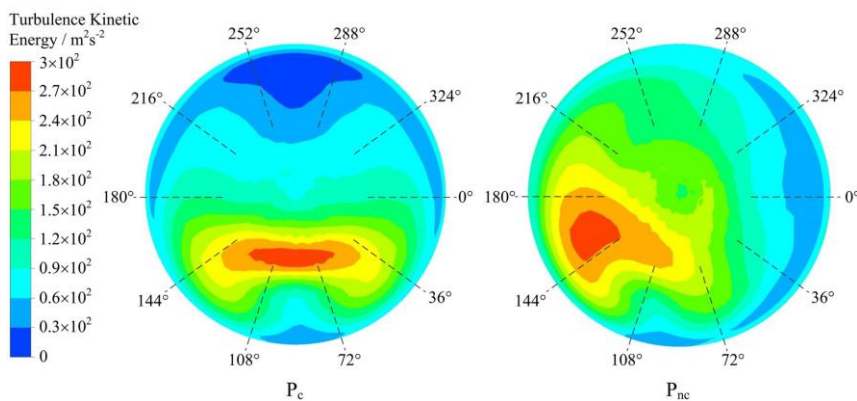
Fig. 22 Variation of the circumferential velocity

Table 6 Average turbulence kinetic energy in sections m_1 and m_2

Inlet pipes	Section	Average turbulence kinetic energy / m^2s^{-2}
P_c	m_1	140
	m_2	102
P_{nc}	m_1	182
	m_2	134

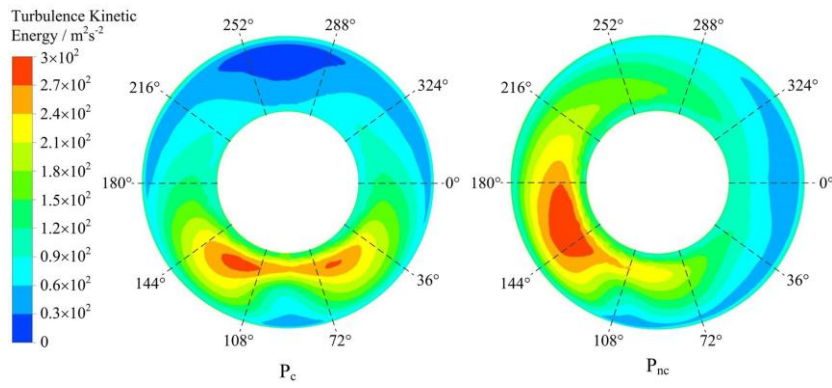


(a) Turbulent kinetic energy distribution within section m_1

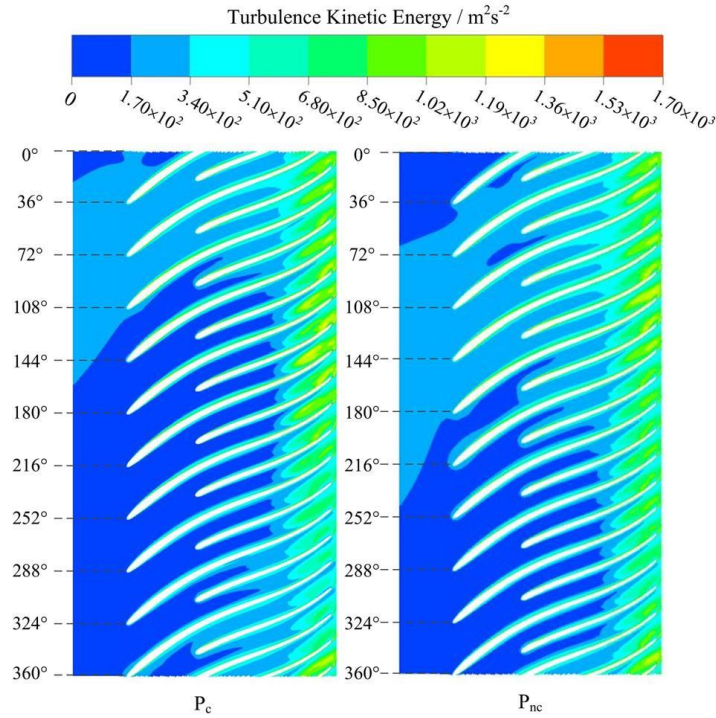


(b) Turbulent kinetic energy distribution within section m_2

Fig. 23 Turbulent kinetic energy distribution within sections m_1 and m_2



(a) Turbulent kinetic energy distribution within the impeller entrance section



(b) Turbulent kinetic energy distribution at span 0.5

Fig. 24 Turbulent kinetic energy distribution within the impeller

characteristics, and this area was positioned in the lower region. The area possessed higher turbulence kinetic energy within sections of P_{nc} was relatively larger compared to that of P_c , while this region exhibited a shift with the same rotation direction of the impeller. However, it consistently maintained a similar distribution pattern to the region with low total pressure in Fig. 13, and the maximum and average turbulence kinetic energy in sections m_1 and m_2 of P_{nc} were both greater than those of P_c , indicating enhanced flow instability within P_{nc} .

Figure 24(a) and (b) depicts the turbulent kinetic energy distribution at the impeller entrance and within half of the blade height (span 0.5) region, respectively. Figure 24 indicated that the region with high turbulent kinetic energy within the impeller entrance section corresponded to the circumferential region within the inlet duct with lower total pressure. The axial velocity of the fluid in this region was relatively lower due to the impact of the swirling flow on the axial motion of the

fluid, thus resulting in some flow losses. Additionally, the adoption of P_{nc} led to a larger area with high turbulent kinetic energy and affected wider flow passages, thereby leading to greater flow losses compared to P_c . The circumferential regions of high turbulent kinetic energy within the impeller passage when using P_c and P_{nc} were distributed at the angles of $36^\circ\text{--}144^\circ$ and $72^\circ\text{--}216^\circ$, respectively. Moreover, the high turbulence kinetic energy region at the impeller entrance section influenced the turbulent kinetic energy distribution within the downstream flow passages, primarily altering the turbulent kinetic energy distribution along the flow direction within the impeller passages, which caused an uneven turbulent kinetic energy distribution among various passages. The non-uniform distribution of the turbulent kinetic energy in the impeller channel with P_{nc} was more notable than that for P_c , resulting in a wider circumferential area of flow losses compared to P_c . Therefore, the centrifugal compressor's performance deterioration extent was more pronounced for P_{nc} .

5. CONCLUSION

In this investigation, the compressible three-dimensional fluid dynamics within the centrifugal compressor was numerically predicted through the resolution of the RANS equations, the closure was realized using the SST $\kappa\text{-}\omega$ turbulence model. The reliability of the numerical approach was validated through the experimentally measured performance. Then, numerical predictions of the flow behavior and performance of the centrifugal compressor connected to various curved intake tubes were conducted. Ultimately, the non-uniform flow within the curved pipeline and their influence on the performance parameters and flow behavior of the centrifugal compressor were investigated. The primary conclusions were outlined below:

(1) The operating performance decreased for both P_c and P_{nc} , with the P_{nc} configuration consistently yielding lower results than P_c . At high rotational velocity scenarios, the pressure ratio for P_c and P_{nc} decreased by approximately 5.7% and 9.8%, respectively, while the efficiency was reduced by approximately 5.3% and 8.7%, respectively.

(2) A flow field distribution with symmetrical swirling flow formed at the outlet section of P_c , while the offset swirling flow field was presented for P_{nc} . In addition, the flow velocity and total pressure within the lower axial area of the pipes were relatively lower in both intake elbows.

(3) The $PCDs$ for P_c and P_{nc} both increased with the increment of the flow rate, while the PSI for P_c and P_{nc} remained relatively stable across various flow rate conditions. For all rotational speed conditions, the $PCDs$ and PSI of P_{nc} were consistently higher than those of P_c . The $PSDI$ for both P_c and P_{nc} showed an increasing trend with the rising flow rate, with the $PSDI$ for P_{nc} consistently higher at each flow rate scenario. For the high flow rate scenario, the maximum $PSDI$ for P_c and P_{nc} reached approximately 0.137 and 0.386, respectively.

(4) The performance deterioration extent for both curved intake pipelines exhibited an exponential correlation with $PSDI$, and the decline extent of the performance parameters both increased with the rising $PSDI$.

(5) The uneven spread of the flow characteristics at the intake pipelines outlet affected the flow characteristics within impeller. The variation regions in total pressure, operating flow rate, and axial velocity within the impeller entrance were similar to the distortion regions at the curved pipelines outlet zone. The flow field variation area within the impeller for P_{nc} was more extensive and the impact extent was more significant compared to P_c , resulting in a more pronounced performance deterioration extent.

ACKNOWLEDGMENTS

This investigation is supported by the Basic Product Innovation Research Program [20221001].

CONFLICT OF INTEREST

The authors have no conflicts to disclose.

AUTHORS CONTRIBUTION

X. Li: Conceptualization, Formal analysis, Investigation, Writing – original draft. **N. Huang:** Project administration. **W. Han:** Resources. **D. Tong:** Methodology. **Y. Zhang:** Funding acquisition. **J. Zhang:** Validation, Writing – review & editing.

REFERENCES

- Ariga, I., Kasai, N., Masuda, S., Watanabe, Y., & Watanabe, I. (1983). The effect of inlet distortion on the performance characteristics of a centrifugal compressor. *Journal of Engineering for Gas Turbines and Power*, 105(2), 223–230. <https://doi.org/10.1115/1.3227406>
- Broatch, A., Ruiz, S., J. García-Tíscar, & Roig, F. (2018). On the influence of inlet elbow radius on recirculating backflow, whoosh noise and efficiency in turbocharger compressors. *Experimental Thermal & Fluid Science*, 96, 224–233. <https://doi.org/10.1016/j.exptthermflusci.2018.03.011>
- Cheng, X. R., Bao, W. R., Fu, L., & Ye, X. T. (2019). Steady characteristics of internal flow in annular casing of nuclear main pump. *Journal of Lanzhou University of Technology*, 45(1), 49–56. <https://doi.org/10.3969/j.issn.1673-5196.2019.01.010>
- Djodikusumo, I., Diasta, I. N., & Sanjaya Awaluddin, I. (2016). Geometric modeling of a propeller turbine runner using ANSYS BladeGen, meshing using ANSYS turboGrid and fluid dynamic simulation using ANSYS Fluent. *Applied Mechanics and Materials*, 842, 164–177. <https://doi.org/10.4028/www.scientific.net/AMM.842.164>
- Engeda, A., Kim, Y., Aungier, R., & Direnzi, G. (2003). The inlet flow structure of a centrifugal compressor stage and its influence on the compressor performance. *Journal of Fluids Engineering*, 125(5), 779–785. <https://doi.org/10.1115/1.1601255>
- Grimaldi, A., & Michelassi, V. (2019). The impact of inlet distortion and reduced frequency on the performance of centrifugal compressors. *Journal of Engineering for Gas Turbines and Power*, 141(2), 1–9. <https://doi.org/10.1115/1.4040907>
- Han, F. H., Mao, Y. J., & Tan, J. J. (2016). Influences of flow loss and inlet distortions from radial inlets on the performances of centrifugal compressor stages. *Journal of Mechanical Science & Technology*, 30(10), 4591–4599. <https://doi.org/10.1007/s12206-016-0930-y>
- Jahani, Z., Khaleghi, Z., & Tabejamaat, S. (2022). Using tip injection to stability enhancement of a transonic

- centrifugal impeller with inlet distortion. *Journal of Applied Fluid Mechanics*, 15(6), 1815–1824. <https://doi.org/10.47176/jafm.15.06.1089>
- Jiang, C. L., & Zhu, X. Y. (2022). Structural optimization design and internal flow characteristics analysis of axial flow fan. *Journal of Drainage and Irrigation Machinery Engineering*, 40(7), 707-713. <https://doi.org/10.3969/j.issn.1674-8530.20.0235>
- Kammerer, A., & Abhari, R. S. (2009). Blade forcing function and aerodynamic work measurements in a high speed centrifugal compressor with inlet distortion. *Journal of Engineering for Gas Turbines & Power*, 132(9), 95–105. <https://doi.org/10.1115/1.4000614>
- Kim, Y., Engeda, A., Aungier, R., & Direnzi, G. (2001). The influence of inlet flow distortion on the performance of a centrifugal compressor and the development of an improved inlet using numerical simulations. *Proceedings of the Institution of Mechanical Engineers, Part A: Journal of Power and Energy*, 215(3), 323–338. <https://doi.org/10.1243/0957650011538550>
- Li, C., Bai, S. Z., Li, Y. Z., Zhang, J. J., & Zhang, J. M. (2020). Effects of curved tube intake on centrifugal compressor efficiency. *Internal Combustion Engine & Powerplant*, 37(3), 26–31. <https://doi.org/10.19471/j.cnki.1673-6397.2020.06.005>
- Li, D., Yang, C., Zhou, M., Zhu, Z. F., & Wang, H. (2012). Numerical and experimental research on different inlet configurations of high speed centrifugal compressor. *Science China (Technological Sciences)*, 55, 174–181. <https://doi.org/10.1007/s11431-011-4635-2>
- Li, M. Y., Lu, Y. J., Gong, Z. Q., & Yuan, W. (2006). PIV investigation of the internal flow in an axial flow compressor rotor under inlet distortion. *Journal of Aerospace Power*, 21(003), 461–466. <https://doi.org/CNKI:SUN:HKDI.0.2006-03-004>
- Li, W. X., Li, Z. G., Han, W., Li, D. C., Yan, S. N., & Zhou, J. P. (2025). Study of the flow characteristics of pumped media in the confined morphology of a ferrofluid pump with annular microscale constraints. *Journal of Fluids Engineering*, 147(2), 021201. <https://doi.org/10.1115/1.4066486>
- Li, W. X., Li, Z. G., Han, W., Li, Y. B., Yan, S. N., Zhao, Q., & Gu, Z. Y. (2023a). Pumping-velocity variation mechanisms of a ferrofluid micropump and structural optimization for reflux inhibition. *Physics of Fluids*, 35(5), 052005. <https://doi.org/10.1063/5.0149130>
- Li, W. X., Li, Z. G., Han, W., Tan, S. W., Yan, S. N., Wang, D. W., & Yang, S. Q. (2023b). Time-mean equation and multi-field coupling numerical method for low-Reynolds-number turbulent flow in ferrofluid. *Physics of Fluids*, 35(12), 125145. <https://doi.org/10.1063/5.0179961>
- Li, X., Huang, N., He, K., Tong, D., Zhang, Y. L., & Zhang, J. (2024). On erosion wear of flat specimens incorporating roughness angle correction. *Physics of Fluids*, 36, 109102. <https://doi.org/10.1063/5.0226359>
- Moosania, S. M., & Zheng, X. Q. (2017). Effect of internal heat leakage on the performance of a high pressure ratio centrifugal compressor. *Applied Thermal Engineering*, 111, 317–324. <https://doi.org/10.1016/j.applthermaleng.2016.09.030>
- Nili-Ahmadabadi, M., Hajilouy-Benisi, A., Durali, M., & Ghadak, F. (2008). Investigation of a centrifugal compressor and study of the area ratio and tip clearance effects on performance. *Journal of Thermal Science*, 17(4), 314–323. <https://doi.org/10.1007/s11630-008-0314-1>
- Raman, S., & Kim, H. (2018). Computational analysis of the performance characteristics of a supercritical CO2 centrifugal compressor. *Computation*, 6(4), 54. <https://doi.org/10.3390/computation6040054>
- Sheoran, Y., Bouldin, B., & Krishnan, P. M. (2011). Compressor performance and operability in swirl distortion. *Journal of Turbomachinery*, 134(4), 041008. <https://doi.org/10.1115/GT2010-22777>
- Sun, Z., Wang, B., Zheng, X., Kawakubo, T., & Numakura, R. (2020). Effect of bent inlet pipe on the flow instability behavior of centrifugal compressors. *Chinese Journal of Aeronautics*, 33(8), 2099–2109. <https://doi.org/10.1016/j.cja.2020.02.013>
- Tian, H. Y., Tong, D., Liu, Y., Xing, W. D., Chen, D. F., & Gao, C. (2021a). The effect of blade trailing edge swept on the performance of centrifugal compressor. *Journal of Engineering Thermophysics*, 42, 399–406.
- Tian, H. Y., Hou, K., Tong, D., & Liu, X. Y. (2021b). Effect of inlet end-wall guide vanes on the performance of centrifugal compressor. *Chinese Internal Combustion Engine Engineering*, 42(6), 95–102. <https://doi.org/10.13949/j.cnki.nrgc.2021.06.013>
- Tian, Y. B., Tang, Y. H., Wang, Z. H., & Xi, G. (2017, June 26-30). Influence of adjustable inlet guide vanes on the performance characteristics of a shrouded centrifugal compressor. Proceedings of ASME Turbo Expo 2017: Turbomachinery Technical Conference and Exposition, Charlotte, NC, USA. V02CT44A020. <https://doi.org/10.1115/GT2017-63918>
- Toge, T. D., & Pradeep, A. M. (2017). Experimental investigation of stall inception of a low speed contra rotating axial flow fan under circumferential distorted flow condition. *Aerospace Science and Technology*, 70, 534–548. <https://doi.org/10.1016/j.ast.2017.08.041>
- Tong, D., Tian, H. Y., Liu, X. Y., Liu, Y., Gao, C., & Li, X. (2021). Effect of inlet bend pipe on the centrifugal compressor performance and its optimization design. *Acta Armamentarii*, 42(4), 9. <https://doi.org/10.3969/j.issn.1000-1093.2021.04.004>

- Wang, H. Y., Yang, D. F., Zhu, Z. C., Zhang, H. J., & Zhang, Q. (2023). Effect of interstage pipeline on the performance of two-stage centrifugal compressors for automotive hydrogen fuel cells. *Applied Science-Basel*, 13(1), 503. <https://doi.org/10.3390/app13010503>
- Xin, J. C., Wang, X. F., & Liu, H. T. (2016). Numerical investigation of variable inlet guide vanes with trailing-edge dual slots to decrease the aerodynamic load on centrifugal compressor impeller. *Advances in Mechanical Engineering*, 8(3), 1–14. <https://doi.org/10.1177/1687814016640653>
- Xu, Z. L., Da, X. Y., & Fan, Z. L. (2017). Assessment of swirl distortion of serpentine inlet based on five-hole probe. *Acta Aeronautica et Astronautica Sinica*, 38(12), 53–62. <https://doi.org/10.7527/S1000-6893.2017.121342>
- Xu, Z. L., Gao, R. Z., & Da, X. Y. (2018). Assessment and measurement of total pressure distortion based on five-hole-probe for S-shaped inlet. *Journal of Experiments in Fluid Mechanics*, 32(4), 78–86. <https://doi.org/CNKI:SUN:LTLC.0.2018-04-010>
- Yan, C., Yu, J., Xu, J. L., Fan, J. J., & Gao, R. Z. (2011). On the achievements and prospects for the methods of computational fluid dynamics. *Advances in Mechanics*, 41(5), 562–589. <https://doi.org/10.6052/1000-0992-2011-5-lxjzj2010-082>
- Zhang, W., Wang, Y., & Xu, Z. (2001). Experimental study progress of internal flow and rotor/stator interaction in turbomachinery. *Fluid Machinery*, 29, 6–10. <https://doi.org/10.3969/j.issn.1005-0329.2001.08.001>
- Zhao, B., Sun, H., Wang, L. L., & Song, M. X. (2017). Impact of inlet distortion on turbocharger compressor stage performance. *Applied Thermal Engineering*, 124(1), 393. <https://doi.org/10.1016/j.applthermaleng.2017.05.181>
- Zhou, S. D., & Wen, Q. (2005). The effect of inlet total pressure radial distortions on the performance characteristics of a centrifugal compressor. *Gas Turbine Experiment and Research*, 18(3), 5. <https://doi.org/10.3969/j.issn.1672-2620.2005.03.003>